

pubs.acs.org/JACS Article

Exploring the Activation Process of the Glycine Receptor

Junfang Yan, Luonan Chen,* Arieh Warshel,* and Chen Bai*



Cite This: J. Am. Chem. Soc. 2024, 146, 26297-26312



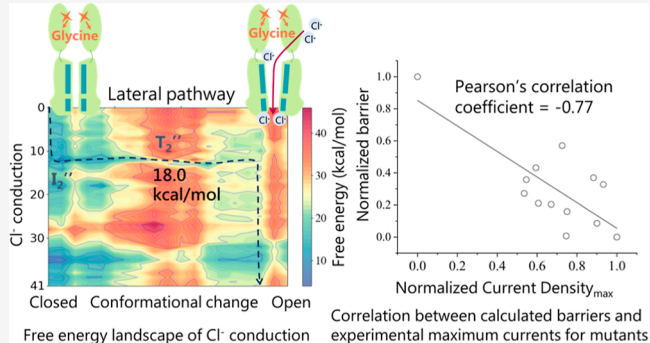
ACCESS I

Metrics & More

Article Recommendations

Supporting Information

ABSTRACT: Glycine receptors (GlyR) conduct inhibitory glycinergic neurotransmission in the spinal cord and the brainstem. They play an important role in muscle tone, motor coordination, respiration, and pain perception. However, the mechanism underlying GlyR activation remains unclear. There are five potential glycine binding sites in α 1 GlyR, and different binding patterns may cause distinct activation or desensitization behaviors. In this study, we investigated the coupling of protein conformational changes and glycine binding events to elucidate the influence of binding patterns on the activation and desensitization processes of α 1 GlyRs. Subsequently, we explored the energetic distinctions between the apical and lateral pathways during $\alpha 1$ GlyR conduction to identify the pivotal factors in the ion conduction



Free energy landscape of Cl- conduction

experimental maximum currents for mutants

pathway preference. Moreover, we predicted the mutational effects of the key residues and verified our predictions using electrophysiological experiments. For the mutants that can be activated by glycine, the predictions of the mutational directions were all correct. The strength of the mutational effects was assessed using Pearson's correlation coefficient, yielding a value of -0.77between the calculated highest energy barriers and experimental maximum current amplitudes. These findings contribute to our understanding of GlyR activation, identify the key residues of GlyRs, and provide guidance for mechanistic studies on other pLGICs.

INTRODUCTION

Glycine receptors (GlyRs) belong to the pentameric ligandgated ion channels (pLGICs). With other pLGICs, such as nicotinic acetylcholine receptors (nACHRs), serotonin-3receptors (5-HT3R), γ-aminobutyric acid-A-receptors (GA-BA_AR), and zinc-activated channel (ZAC), they are important in intercellular communications in the nervous system. 1-4 Similar to GABAAR, GlyRs function at inhibitory synapses in the human body, mediate glycinergic neurotransmission in sensory and motor neurons (in the spinal cord and brainstem), and play vital roles in muscle tone, motor coordination, respiration, and pain perception. 5-8 It has been broadly reported that GlyRs stay in the closed state without agonists bound, and the binding of glycine to the extracellular interface of the two subunits (Figure 1b,c) can help stabilize the open state (ion-conductive state).9 However, repetitive or prolonged binding of glycine can trigger a conformational change from the open state to the desensitized state where ions can hardly be conducted.^{9,10} A diverse array of agents, including neurosteroids, cannabinoids, metal ions, toxins, and certain general anesthetics (volatile compounds, such as desflurane and chloroform), have been demonstrated to modulate GlyRs. 11-15 Dysfunction of GlyRs could cause severe diseases, including hyperekplexia. 16-23 Recent studies have presented that mutations in the human GlyR $\alpha 1$ and β subunits are the primary causative factors for startle disease. 16-23 The ability of GlyRs to inhibit nociceptive signals within the dorsal horn of

the spinal cord and their function in the motor reflex circuits of the spinal cord have led to the emergence of GlyRs as potential therapeutic targets for pain alleviation, muscle relaxation, and other diseases. 12,14,24-2

GlyRs are pentamers comprising different subunits that assemble in various forms, including homomers comprising solely of α subunits or heteromers comprising α and β subunits.²⁸ The predominant subunit stoichiometry is $4\alpha:1\beta$ for heteromeric receptors.²⁹ Each subunit contained a transmembrane domain (TMD) formed by four α -helical bundles (M1-M4), an extracellular domain (ECD) folded into a twisted ten-strand β -sheet, and an unresolved intracellular domain (ICD) located between M3 and M4 (Figure 1b,c).³⁰ The transmembrane ion conduction pore of GlyRs is formed by the M2 helices of the five subunits, which is important for GlyR selectivity for anions, 31 receptor activation, and desensitization.³² One question is how anion/cation discrimination is achieved. Research has shown that the charge selectivity filter of $\alpha 1$ GlyR is in the region of the -1' and -2'positions (residues in pore-lining M2 helices, Figure 1d). This

Received: June 23, 2024 Revised: September 6, 2024 Accepted: September 6, 2024 Published: September 16, 2024





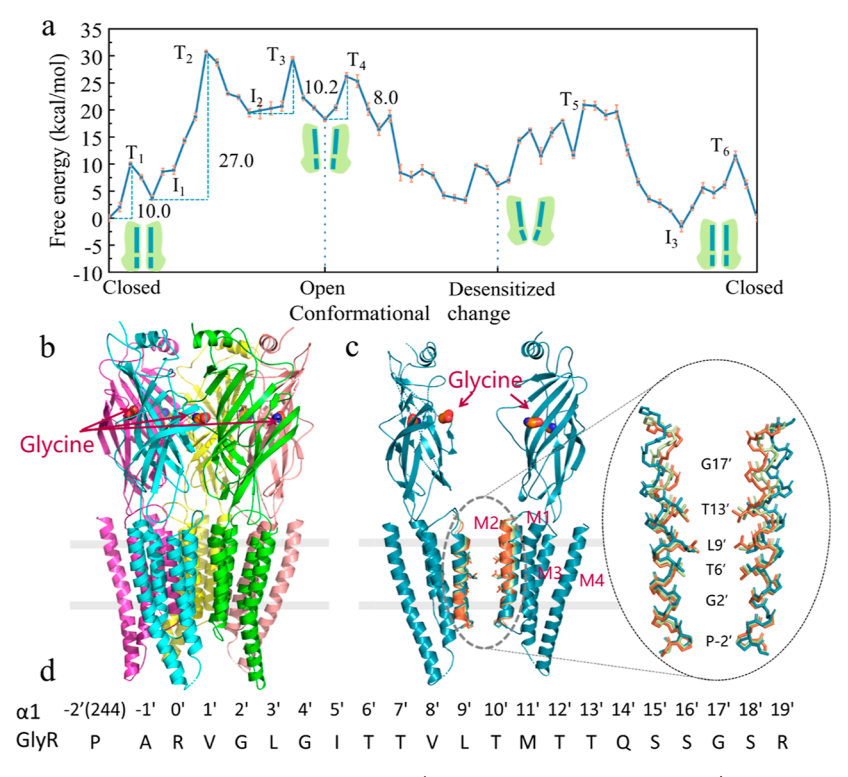


Figure 1. (a) CG free energy profile of α 1 GlyRs in the gating cycle (closed-open-desensitized-closed) without agonist binding, with the free energy of the closed state set to zero. I and T denote different intermediate and transition states, respectively. The four energy barriers from the closed to open state and from the open to desensitized state are marked with dashed lines and the corresponding numerical values. Error bars are colored in orange. Green cartoons represent conformational differences in each state. (b) Structure of α 1 GlyR. Glycine molecules bind to the interface between the two subunits. The position of the membrane is denoted in gray. (c) M2 helical orientations in closed (orange), T_2 (green), and open (teal) states. For clarity, only two nonconsecutive GlyR subunits (teal cartoons) complexed with glycine ligands (spheres) in the open state are shown. M2 helices are magnified with licorice back presentation. For residues whose side chains face the channel pore, all heavy atoms are shown in licorice, with the residue label corresponding to the sequence in panel d. (d) Residues sequence lining the M2 helix. The intermediate positively charged R in the M2 helix was designated 0'. The residue index of the -2' position was 244 in our calculation.

was evidenced by the observation that the mutation from A to E in the -1' region (residues in pore-lining M2 helices, Figure 1d) was sufficient to convert $\alpha 1$ GlyR into a cation-selective channel. 33,34 In addition, Cymes et al. proposed that not only the charge sign of ionized residues but also the orientation of the ionized side chains determine the charge selectivity for GlyRs. 35,36 Regarding the activation and desensitization of GlyRs, it was demonstrated that the upper part of the channel carries the activation gate, with the 9' residue (residues in pore-lining M2 helices, Figure 1d) serving as the bottom end of the activation gate. 37,38 The desensitization gate was identified at the intracellular end of the pore (between positions -3' and 4' (residues in pore-lining M2 helices, Figure 1d)) in proximity to the selectivity filter. 39,40

GlyRs are among the most extensively studied proteins within the pLGIC family. Recently, GlyR structures in multiple states complexed with diverse agonists, antagonists, and modulators have been determined. $^{15,29,41-49}$ Du and coworkers were the first to obtain full-length electron cryomicroscopy structures of zebrafish $\alpha 1$ GlyR bound to strychnine, glycine, or glycine/ivermectin. 41 A study by Kumar et al. reported $\alpha 1$ GlyR structures with Δ -tetrahydrocannabinol (one of the cannabinoids) binding at the TMD in multiple conformational states, elucidating the molecular basis for cannabinoid-mediated potentiation of GlyR. 45 In GlyR activation, Glycine binding is a preliminary process, triggering subsequent GlyR conformational changes and Cl $^-$ conduction. 44,50 It has been postulated that an

intermediate closed state exists between closed and open states that lasts longer with partial agonist binding, while it lasts shorter with glycine binding. $^{50-53}$ It is encouraging to note that Yu et al. reported the predicted intermediate closed state structures with GABA or taurine (partial agonists) binding, hinting that the intermediate closed state of GlyRs with glycine binding exists before full activation and is short-lived and hard to detect. They also successfully determined zebrafish $\alpha 1$ GlyR structures in open and desensitized states with taurine, GABA, or glycine binding. 44 These structures provide the opportunity to employ advanced modeling and simulation tools to investigate these systems.

The activation of GlyRs is a complex physiological process influenced by numerous factors, including the type 44,55,56 and the number of agonists. For homomeric α1 GlyRs, there are five equivalent binding sites, each of which can bind one glycine molecule as an agonist. Agonists generate currents that may be single or bursting in nature. Bursts are defined as groups of currents separated by relatively long periods of closure. S8,59 One noteworthy phenomenon in GlyR activation is the observation of at least three distinguishable open states with varying mean burst durations. The burst duration distributions exhibited concentration-dependent behavior, with long bursts being generated at high glycine concentrations and short bursts being more frequent at low glycine concentrations. In their study, Beato et al. proposed that any number of glycine molecules from one to five can open the channel, although with varying degrees of efficiency. They further

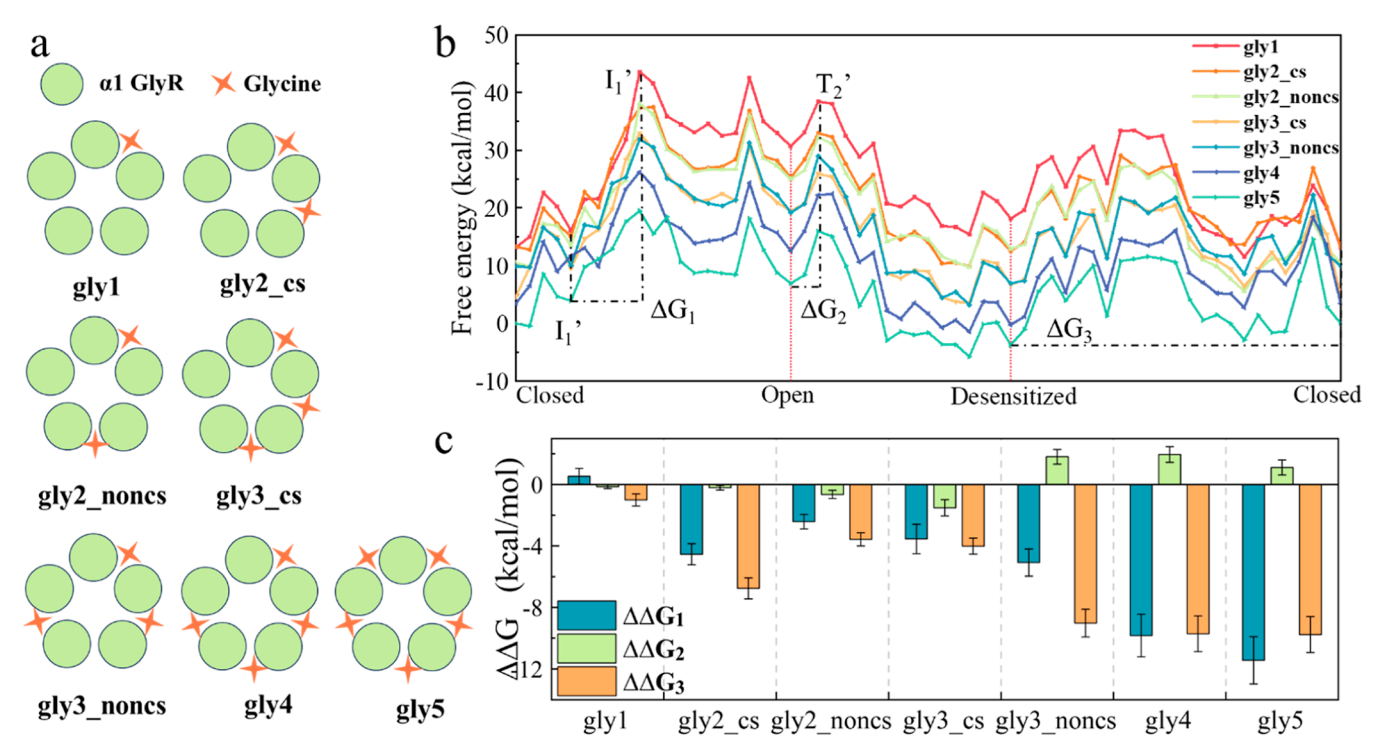


Figure 2. (a) Seven glycine binding patterns; the star designates glycine, and the green cycle denotes the α1 GlyR subunit. (b) Coupled free energy profile of conformational change and glycine binding for all glycine binding patterns. For each situation, ΔG_1 is the activation barrier, ΔG_2 is the desensitization barrier, ΔG_3 is the energy difference between the closed and desensitized states ($\Delta G_3 = G_{\text{desensitized}} - G_{\text{closed}}$). (c) Three key ΔG changes result from different glycine binding patterns compared to the apo states. $\Delta\Delta G = \Delta G_{\text{bind}} - \Delta G_{\text{apo}}$ X-axis represents various possible glycine binding patterns, whereas Y-axis stands for ΔG changes in kcal/mol. Error bars are colored in black.

suggested that at least three glycine molecules were required for the effective opening of $\alpha 1$ GlyRs. ^{24,57,61,62} Nevertheless, the impact of varying glycine molecule binding on GlyRs activation and desensitization behaviors remains unclear, prompting further investigation into the relationship between ligand binding amounts and activation/desensitization behaviors.

Computational studies have sought to elucidate the mechanisms of the action of GlyR. One issue that requires further investigation is the selectivity between lateral and apical pathways. Cerdan et al. proposed that lateral fenestration, rather than apical entrance, is the major extracellular permeation pathway based on molecular dynamics (MD) simulations and validated this hypothesis through electrophysiological experiments.⁶³ Nevertheless, the authors did not give explanations for the pathway preference from a structural and energetic perspective. Furthermore, Cerdan et al. demonstrated that a previously reported "open" structure could not represent the physiologically active state, 64 as it rapidly collapsed in MD simulations and displayed an ion pore with a minimum diameter of 8.2 Å, ³⁰ larger than conventional 5.3 Å.31 Subsequently, Damgen et al. used MD simulations to capture a stable open state structure that could avoid collapse in 300 ns simulations.65

In this study, we investigated GlyR activation and conduction. Given the considerable computational cost for GlyRs with about two thousand residues, we used the coarsegrained (CG) model,66-70 which has been previously used in the context of electrostatic energetics and the generation of free energy surfaces. The ionization states of the charged residues were determined using the Metropolis Monte Carlo Proton Transfer approach in the CG method.⁶⁹ The method

encompasses a multitude of considerations beyond the mere modeling of Coulombic interactions between charged species. It also accounts for the environmental solvation effect exerted by nearby polar and nonpolar residues, including the contributions from the solvation of charged species.⁷¹ The CG model has been successfully employed in the simulation of several systems, including the activation of β 2AR,⁷² the protomotive vectorial motion of ATPase, 73,74 and the prediction of the mutational effects of SARS-CoV-2 variants. 75,76

In our work, we used the CG model to investigate the free energy landscape and elucidate the activation and desensitization barrier changes under distinct binding patterns. This approach enabled us to determine the energetic and structural changes in GlyR activation and desensitization processes with varying amounts of glycine molecules binding. Moreover, we calculated the energy difference in the chloride ion conduction between the apical and lateral pathways. We elucidated the rationale behind the preference for lateral pathways and proposed that the electrostatic environment plays a pivotal role in determining the pathway choice. Finally, we identified novel mutational sites that could influence GlyR conduction based on the acquired kinetic information, including the transition state structure, reaction barrier, free energy change, and ratedetermining step. These predictions were further validated by electrophysiological experiments and exhibited excellent performance. This work has advanced our understanding of GlyRs and other pLGICs' biological mechanisms from a physical chemistry perspective, rather than solely observing their physiological behavior.

RESULTS

the real pathway.

Change. To explore the conformational free energy landscape, we constructed the models using existing cryo-EM structures to explore the conformational free energy landscape. The closed state (PDB ID 6plz), open state (PDB ID 6ply), and desensitized state (PDB ID 6plx) structures were obtained from the Protein Data Bank (PDB) database.44 After the implementation of energy minimization and relaxation procedures to eliminate potential steric clashes of our models, intermediate structures between each major state were generated by the "Targeted molecular dynamics" (Targeted MD) method to depict the complete thermodynamic cycle. For each structural transition, 19 intermediate structures were selected at equal intervals to reproduce the free energy profile, as illustrated in Figure 1a (Further details provided in the

Methods section). However, channel opening, closing, and

desensitization are complex processes that involve large

conformational changes. The pathway obtained by the

Targeted MD method offered us a reasonable estimate of

CG Free Energy Profile for α 1 GlyR Conformational

Figure 1a depicts the free energy profile of GlyRs during the gating cycle in the absence of agonists in the binding pocket (apo state). From the closed to open state, the M2 helices move outward allowing chloride conduction (Figure 1c). Conversely, during the transition from the open to the desensitized state, as illustrated in the accompanying cartoons, the intracellular end of the pore contracts ultimately leading to the complete closure of the channel (Figure 1a). The closedto-open-state conversion involves three distinct barriers, with the second barrier being the most significant (27.0 kcal/mol) and thus the rate-determining step of the conformational change. The first barrier (10.0 kcal/mol) is produced by the reorganization of the loops in the ECD, whereas the two latter barriers arise from the outward orientation of the M2 helices (Figure 1c). The contribution of each residue to the highest barrier was calculated (Figure S3). The result revealed that residue R265 in the upper part of the M2 helix (19' in Figure 1d) and R309 in the lower part of the M4 helix make critical contributions to the I₁-T₂ barrier. From the open to the desensitized state, the highest barrier is 8.0 kcal/mol, which may be induced by the early stage conformational changes that could lead to further structural conversion. Figure S3 presents the results of the energy analysis, which indicate that D278 in the M3 helix exerts the most positive influence on the open-T₄ barrier. In brief, residues R265, D278, and R309 play crucial roles in the transition of GlyR gating cycle.

Coupling between the Conformational Change and **Glycine Binding.** One crucial issue is the influence of varying amounts of glycine binding on the α 1 GlyR activation kinetics. Previous studies have indicated that any number of glycine molecules, ranging from one to five, can open the ion channels with different efficiency. 24,57 However, the effect of ligand number on the activation mechanism remains largely unknown. al GlyR has five potential binding sites with seven glycine binding patterns (Figure 2a). To elucidate the nuances of the alterations in the activation and desensitization behaviors across the seven distinct glycine binding patterns, we constructed conformational free energy profiles with glycine binding under each of the seven conditions. For each intermediate structure obtained by the Targeted MD method,⁷⁷ the glycine molecules were docked to the binding sites and followed by 6 ns relaxation. The binding free energy was subsequently calculated using the PDLD/s-LRA/β method, 78-80 as detailed in the Methods section.

All seven free energy curves that coupled the conformational changes and glycine binding are shown in Figure 2b. The Xaxis represents the coordinates of the conformational changes, whereas the Y-axis denotes the conformational free energy plus glycine binding free energy change for each binding pattern. The slanted prime symbols in I' and T' were employed to differentiate these states from those depicted in Figure 1a. To provide further insight into the influence of varying glycine binding on α 1 GlyR activation and desensitization kinetics, we focus on the reaction barrier changes. For this analysis, key ΔG changes resulting from different glycine binding patterns comparing with apo states (states with no glycine bound) are illustrated in Figure 2c. The formula for calculating the change in Gibbs free energy is as follows: $\Delta \Delta G =$ $\Delta G_{\text{bind}} - \Delta G_{\text{apo}}$. Here ΔG_{bind} denotes the Gibbs free energy change associated with the binding pattern represented on the X-axis. $\Delta \Delta G_1$ represents the change in the activation energy barrier, $\Delta \Delta G_2$ indicates the change in the desensitization barrier, and $\Delta \Delta G_3$ denotes the change of the energy difference between the closed and desensitized states (G_{desensitized}- G_{closed}). Finally, the three $\Delta\Delta G$ changes provided critical information regarding the barriers involved in different glycine binding patterns, which can be used to analyze the activation and desensitization behavior at different concentrations of glycine.

The results indicate that (1) the activation barrier decreases with increasing glycine molecules; (2) although the desensitization barrier initially decreased, it ultimately increased when more glycine molecules were bound; and (3) the desensitized state energy continuously decreased and ultimately became lower than that in the closed state with increasing glycine molecules (Table S2). Beato et al. showed that the open duration time was prolonged as the glycine concentration was elevated through electrophysiological experiments with varying concentrations of glycine and correlation analysis to assess the mean open and shut times. 24,57 Our results are consistent with those of previous experiments in that a higher glycine concentration typically indicates a greater number of glycine molecules bound, whereas a reduction in the activation barrier or an increase in the desensitization barrier would cause GlyRs remaining in the open state for a longer period. In addition, Colquhoun et al. proposed that desensitization is pronounced at elevated glycine concentrations.^{9,24} In our study, the energy in the desensitized state was the lowest (Tabel S2b) among all three states when the binding glycine number reached its maximum (five), indicating that the desensitized state was the predominant state at high glycine concentrations from a thermodynamic perspective. These results demonstrated a substantial concordance between the calculated and experimental outcomes. The current results also indicate that increasing the concentration of glycine facilitates activation and impedes desensitization of GlyRs. As shown in Table S2b, when the number of binding glycine molecules is greater than or equal to three (binding at nonconsecutive sites), the activation barrier drops below 22.0 kcal/mol and GlyR achieves an efficient opening. The magnitude of the activation energy barrier is comparable to that of the bestrophin-1 channel proteins (23.8 kcal/mol), which is also a pentamer with five subunits surrounding a central pore and conducts chloride ions, highly resembling GlyRs.⁸¹

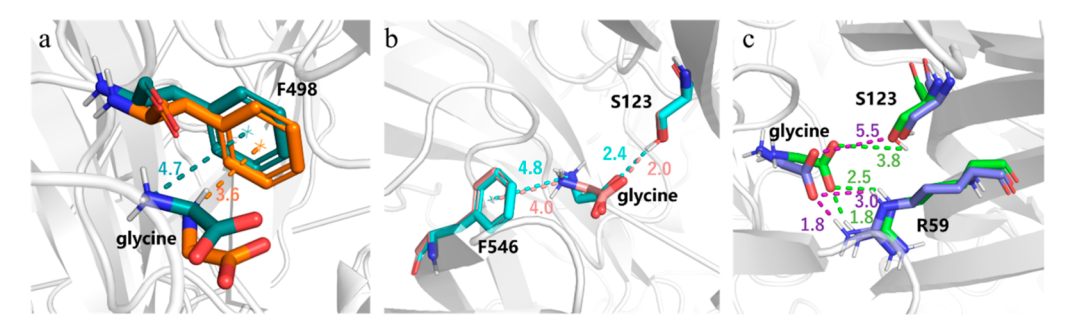


Figure 3. Top view of the distances between glycine and important residues in the binding pocket in different conformational states. (a) The distances between the ammonium N atom of glycine and the center of benzene of F498 for I'_1 (teal) and T'_1 (orange) states. (b) The distances between the carboxyl O1 atom of glycine and the hydroxyl HG atom of S123; the distance between the ammonium N atom of glycine and the center of benzene of F546 for the open (cyan) and T'_2 (salmon) states. (c) Distance between the carboxyl O1 atom of glycine and the hydroxyl HG atom of S123; the distance between the carboxyl O2 atom of glycine and amine HE, HH11 atom of R59 for closed (purple) and desensitized (green) states.

To ascertain the principal contribution to the changes in the energy barriers (ΔG), we measured the distance between glycine and the crucial residues, as well as their orientations within the binding pocket in different conformational states. Our findings indicated that the distance between the ammonium N atom of glycine and the center of the benzene ring of F498 in the T'_1 state was less than that in the I'_1 state (Figure 3a). Stronger cation– π interactions appear to stabilize the T_1' state and decrease ΔG_1 . The data also suggested that as the protein transitions from the open (salmon) to the T₂' (cyan) state, the hydrogen bond interactions between the carboxyl O1 atom of glycine and the hydroxyl HG atom of S123, and the cation $-\pi$ interaction between the center of benzene of F546 and the ammonium N atom of glycine became weaker (Figure 3b). The weaker interactions between glycine and the protein in the T_2' state will increase the free energy of the T_2' state, which explains the increase in ΔG_2 . Specifically, the two strengthened H-bond interactions between the carboxyl O1 atom of glycine and the hydroxyl HG atom of S123, as well as the carboxyl O2 atom of glycine and the amine HE atom of R59 (Figure 3c), stabilized the desensitized state (green) and thus made it the most stable state among all three states. The energy contributions of each residue to the changes in the barriers indicated that different residues played diverse roles (stabilizing or destabilizing) in different energy barriers, including R59, R113, S123, D436, E496, F498, and F546, as shown in Figure S4. In total, the distinct glycine binding modes in different conformational states resulted in changes in the three energy barriers.

Coupling between the Conformational Change and Chloride Ion Conduction. Besides investigating the conformational changes in the GlyR, we also examined the details of the ion conduction process within GlyR. The objective was to address two key questions: 1. What does it cause relative preferences of the lateral and apical pathways? 2. At what stage is the chloride ion able to pass through a narrow tunnel? A recent study conducted by Cerdan and co-workers has proposed that the lateral pathway functions as the primary chloride extracellular pathway rather than the commonly believed apical entrance. 63 Furthermore, they predicted and validated mutations that can reduce Cl⁻ ion conductance.⁶³ Nevertheless, no study has yet explored this issue from the perspective of free energy. To investigate the structural and free energy distinctions between the apical and lateral pathways in chloride ion conduction, we generated a two-dimensional

free energy landscape that couples the protein conformational change, glycine binding, and chloride conduction processes for both pathways. To identify the potential ion conduction pathway, the chloride ions were positioned within an interval of 2 Å through the channel for each intermediate structure. For each combination of the intermediate conformation and Cl⁻ ion position, a 6 ns MD relaxation was first performed, and the binding free energy of the ion was then calculated using the PDLD/S-LRA/ β method. The same approach has been used in related studies of ion channels. Further details can be found in the Methods section.

The free energy map shown in Figure 4c,d is defined by the X-axis, which represents the conformational change of the GlyR (reaction coordinate, including glycine binding), and the Y-axis, which indicates Cl⁻ conduction from the extracellular end to the intracellular end. The minimum energy pathway from the extracellular to the intracellular vestibule of the channel pore is denoted by black dashed lines. Similarly, the double prime symbols in I" and T" were used to differentiate these states from those depicted in Figures 1a and 2b. The apical and lateral pathways originate from disparate entrances and meet at point T_1 ", where they subsequently share the same pathway until the exit (Figure 4a). As the apical and lateral pathways use the same pathway after point T₁", the 2D energy map below point T_1'' was the same for the apical and lateral pathways. Glycine binding occurs before the conformational change of GlyRs; therefore, glycine binding energy is considered for each point of Figure 4c,d. For the activation process of GlyRs in the main pathway (lateral pathway), chloride ion conduction happens first. Chloride ions are conducted from the entrance to I_1'' point, followed by the conformational change from the closed to open state, and finally the Cl⁻ ions are conducted to the intracellular end (Figure 4d).

To investigate the size differences between the apical and lateral pathways, we used the HOLE program 84 to measure the pore radii of the two pathways in the conformational state of point T_1'' . T_1'' was chosen as the state of interest because Cl^- ions can be conducted in both pathways in this conformational state. Although the lateral pathway is more constricted in the upper portion, the narrowest point has a radius exceeding 1.8 Å, which is larger than the radius of a Cl^- ion ($\sim 1.7-1.8$ Å). This allowed for the conduction of Cl^- ions. In the apical pathway, the upper channel is considerably larger, and constriction occurs exclusively at the intracellular end of

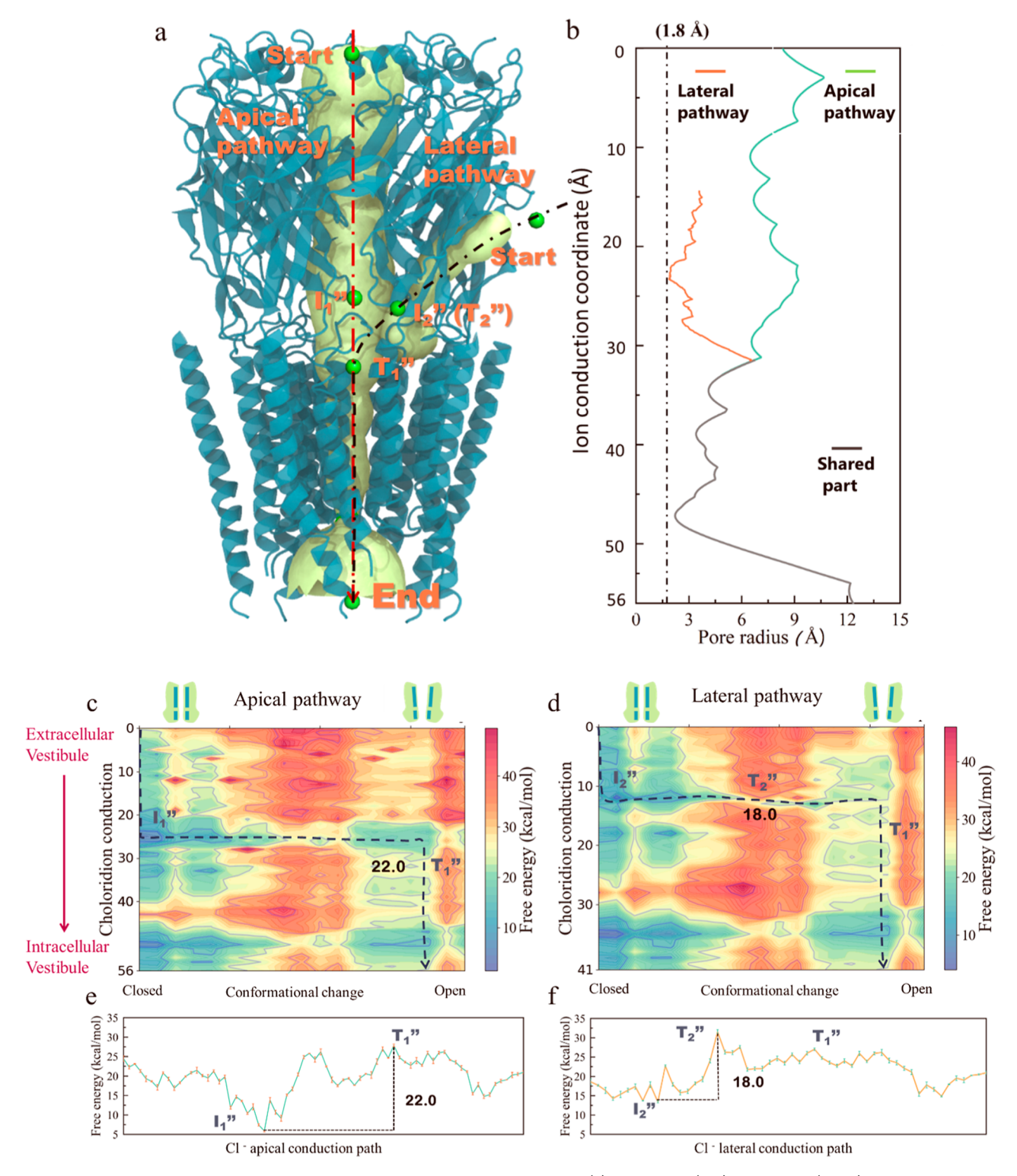


Figure 4. Comparison between apical and lateral paths in chloride ion conduction. (a) The apical (red) and lateral (black) paths in α 1 GlyR, the show the positions of Cl⁻ in the channel for specified states illustrated in panels c and d. (b) The channel pore size along the apical (teal) and lateral pathway (orange) in the conformational state of point T_1'' , the upper limit of chloride ion radius (1.8 Å) is denoted in dashed lines. (c,d) Free energy landscape for Cl⁻ ion conduction via the apical permeation (c) or lateral entrance (d) from the extracellular vestibule to the intracellular end. The least-energy path is shown by bold black dashed lines with overall energy barriers (kcal/mol) in numerical values. (e,f) Free energy profiles along the minimal-energy apical (e) or lateral (f) pathways, with the energy barriers labeled as dashed lines and numerical values. The numbers and capitals strictly correspond to the least-energy path in the apical (c) or lateral pathway (d).

TMD, which is the shared portion of the apical and lateral pathways. The findings suggested that both pathways permit chloride ion conduction in terms of pore size.

As the energy profiles along the minimal-energy Cl⁻ ion conduction pathway (Figure 4e,f) show, the slightly higher energy barrier in the apical pathway (~22 kcal/mol, Figure 4e)

than in the lateral pathway (~18 kcal/mol, Figure 4f) results in the latter pathway acting as the dominant pathway for conducting Cl⁻ ions through the cell membrane. To gain further insight into the distinctions between the two pathways, we decomposed the total free energy change into three components: the free energy change associated with the conformational state, binding free energy change between glycine and GlyR, and binding free energy change between Cl⁻ ions and GlyR (Table 1). The table demonstrates that the

Table 1. Free Energy Decomposition in $I_1''-T_1''$ and $I_2''-T_2''$ Conversions in Figure 4c,d (kcal/mol)

conversion	$\Delta G_{ ext{conf}}^{a}$ (kcal/mol)	$\Delta G_{\rm glycine}^{b}$ (kcal/mol)	$\frac{\Delta G_{ ext{chloride ion}}}{ ext{(kcal/mol)}}^{c}$	ΔG^d (kcal/mol)
$I_1''-T_1''$	17.9	-8.4	12.5	22
$I_{2}''-T_{2}''$	28	-8.8	-1.2	18

"Free energy change of the conformational state. ^bBinding free energy change of glycine molecules to GlyR. ^cBinding free energy change of chloride ions to GlyR. ^dTotal energy change.

higher energy barrier in the apical pathway ($I_1''-T_1''$ conversion in Table 1) is a consequence of the considerably more unfavorable Cl^- ions binding energy difference (+12.5 kcal/mol) than in the lateral pathway ($I_2''-T_2''$ conversion in Table 1, -1.2 kcal/mol).

Previous studies have demonstrated the significance of the electrostatic environment for anion conduction. ^{20,32,85,86} Here we investigate why the Cl⁻ ions binding energy undergoes a notable change during $I_1'' - T_1''$ conversion in the apical pathway, which is the main reason for the higher energy barrier of the

apical pathway. This change can be analyzed by focusing on the difference in the electrostatic potential surface between structures in points I_1'' and T_1'' . As illustrated in Figure S5,b, the Cl⁻ ion at point I₁" was surrounded by a strongly positively charged environment, whereas the environment around position T_1'' was not as much positively charged. This suggests that the difference in the electrostatic environment is an important factor. Furthermore, the energy contribution of each residue to $\Delta G_{\text{chloride ion}} (T_1'' - I_1'')$ in Figure S5c,d indicates that a great number of positively charged residues are present near point I_1'' , whereas a smaller number are found near point T_1'' . This also accounts for the large increase in Cl⁻ binding energy difference from I_1'' to T_1'' . Consequently, the electrostatic environment is of considerable consequence in the substantial Cl^- ion binding energy alteration during the $I_1''-T_1''$ transition. Further, it is of paramount importance to determine the pathway preference of ions.

Mutational Effects of Key Residues of $\alpha 1$ GlyRs. In previous sections, we elucidated the mechanism of activation and chloride ion conduction of GlyRs and obtained kinetic information, especially the reaction barriers and transition state structures. This information provides a solid basis for evaluating the effects of mutations on barrier change, which is highly correlated with the speed and effectiveness of the activation process. 72,76,83 In addition, our investigation was not limited to the direction of mutation effects (impeding or promoting the function of GlyRs) but also encompassed the strength of mutational effects.

First, to study the direction of the mutation effects, we calculated the change in the highest barrier after mutation. This was defined as $\Delta\Delta G_4$ = barrier_{mt} $(T_2'' - I_2'')$ - barrier_{wt}

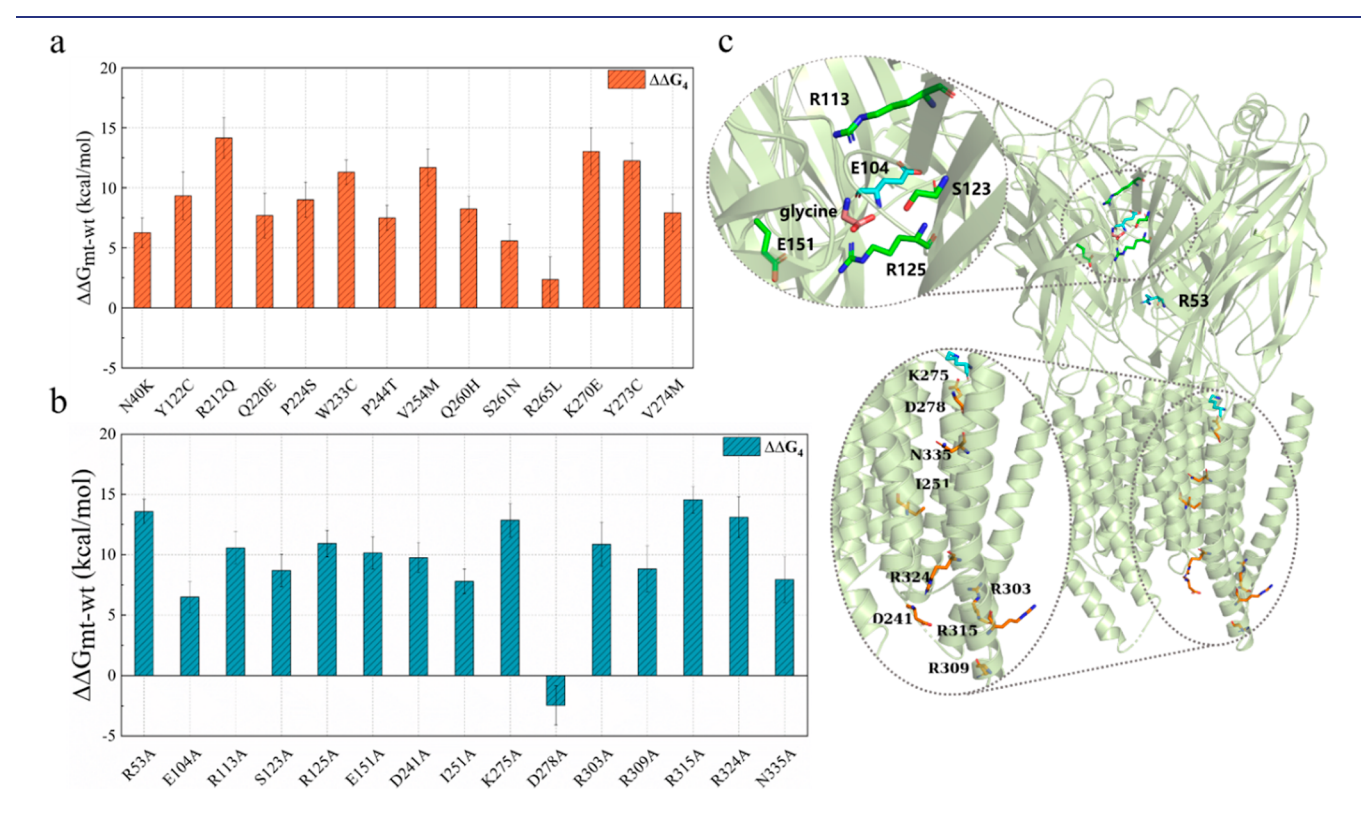


Figure 5. In silico screening of mutations. (a) Computed mutational effects of known mutations that cause hyperekplexia. (b) Alanine scanning calculations for the proposed residues that may influence GlyR function. $\Delta\Delta G_4$ = barrier_{mt} $(T_2''-I_2'')$ -barrier_{wt} $(T_2''-I_2'')$; here, I_2'' and T_2'' states correspond to the states in Figure 4d, "mt" designates mutation type. (c) Positions of mutations in panel b. The residues around glycine (salmon) are colored green, those located in the TMD are colored orange, and the other residues are colored cyan.

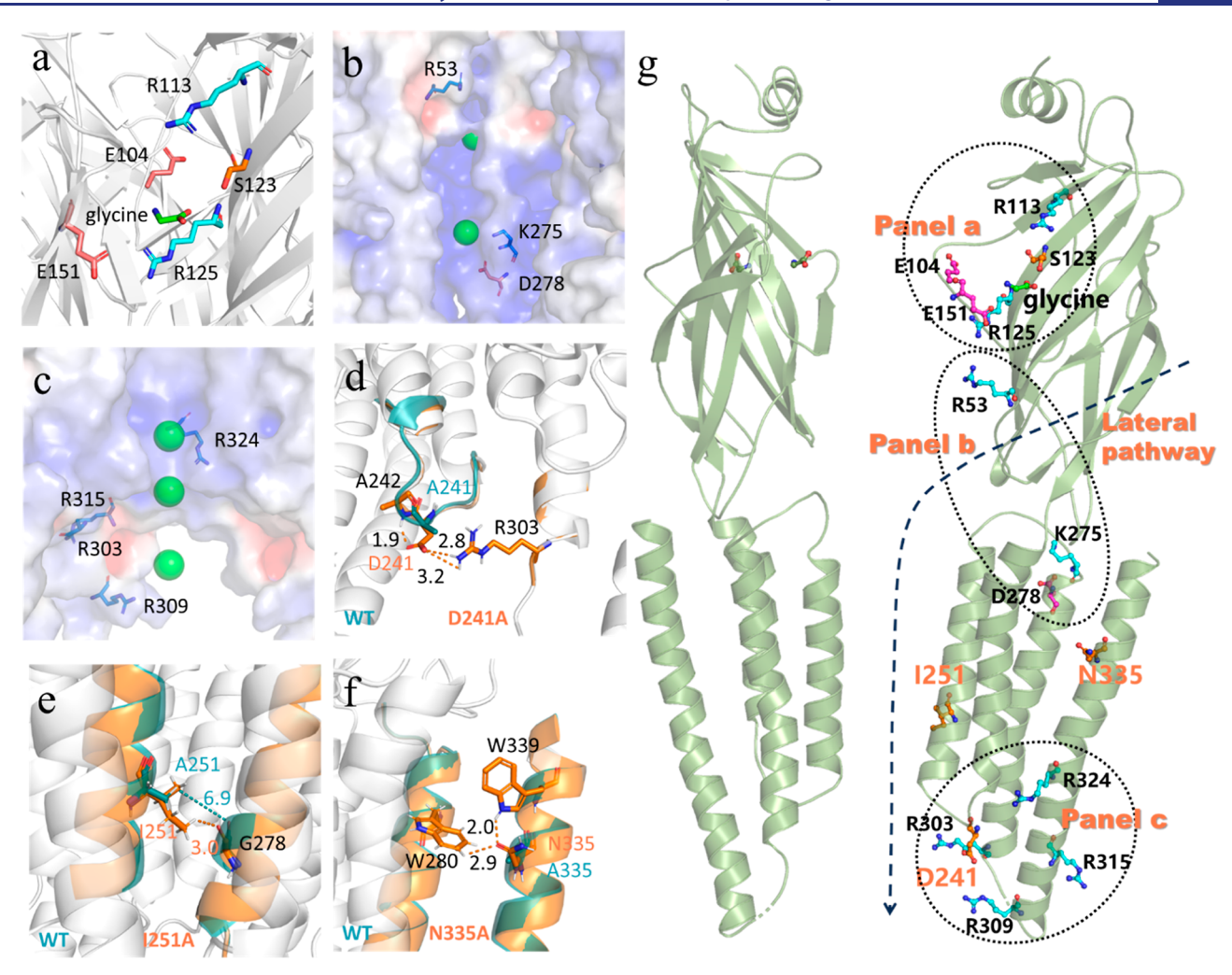


Figure 6. Local interaction environment of residues selected for mutagenesis studies. The chloride ions are shown as green spheres. All structures were at point T₁" in Figure 4d. (a) Residues around glycine binding site. Glycine is denoted and colored in green. Panels b and c show the electrostatic potential surface of the ECD and intracellular end of the TMD, respectively. Positively charged residues or the environment are colored in blue, and negative residues or the environment are colored in red. Local binding environment of (d) D241, (e) I251, and (f) N335. Polar interactions are shown as dashed lines with distances in Å. WT structures are presented in orange, and mutated structures are shown in teal. (g) Two nonconsecutive GlyR subunits (limon cartoons) complexed with glycine ligands (green) are shown to indicate the locations of other panels. The lateral pathway is denoted in black dashed lines. Residues D241, I251, and N335 are labeled and colored in orange. Other residues are labeled in black.

 $(T_2''-I_2'')$, where I_2'' and T_2'' are the two points, as shown in Figure 4d. A positive value of $\Delta\Delta G_4$ indicates a higher activation energy barrier, which impedes chloride ion conduction. Conversely, a negative $\Delta \Delta G_4$ value suggests a lower activation energy barrier, which facilitates the conduction of Cl⁻ ions. Previously identified dominant mutations causing hyperekplexia have been shown to suppress receptor function primarily by disrupting allosteric signal transduction linking agonist binding to channel opening.⁸⁷ In our study, those known mutations should correspond to those with a positive $\Delta\Delta G_4$, since they have been demonstrated to have a negative effect on the activation of GlyRs. We initially calculated the barrier changes of the those known mutations to validate the reliability of our methodology by comparing our predictions with the previous findings (Figure 5a). 16,17,19 The results showed that all mutations resulted in a discernible barrier increase, which aligns with experimental observations and validates the reliability of our predictions regarding the directions of the mutation effects.

Second, we investigated the mutational effects of the new residues on the permeation pathway, glycine binding sites, and important loop regions. In the selection of mutational sites, we chose 30 residues in total for alanine scanning calculations (Figure S6). Many factors were considered in the first selection of 30 residues, including their locations, the residue energy contributions to the barriers, and the charge distributions of residues. Then, to decrease the workload of experiments, we selected mutations with $\Delta\Delta G_4 \geq 7.5$ kcal/mol and the only mutation D278A with negative $\Delta\Delta G_4$ to study the mutational effects. The corresponding mutational effects are illustrated in Figure 5b, which indicates that R53A, E104A, R113A, S123A, R125A, E151A, D241A, I251A, K275A, R303A, R309A, R315A, R324A, and N335A inhibit chloride conduction, whereas D278A facilitates chloride conduction.

We endeavored to understand the impact of these mutations on protein functionality from a structural standpoint. Residues E104, R113, S123, R125, and E151 were identified in the glycine binding site (Figure 6a). The interactions between the ligand and residues stabilize the receptor in the open state,

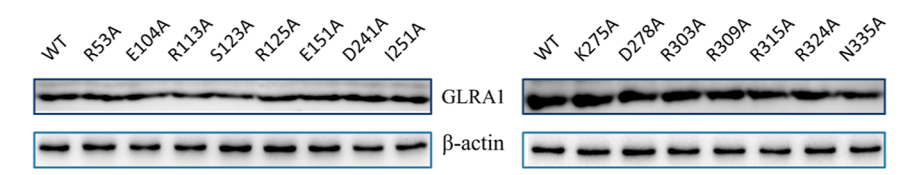


Figure 7. Western blot images of α 1 GlyR expression in the wild type and 15 mutants in HEK293T cells. β -Actin expression was detected in the control group.

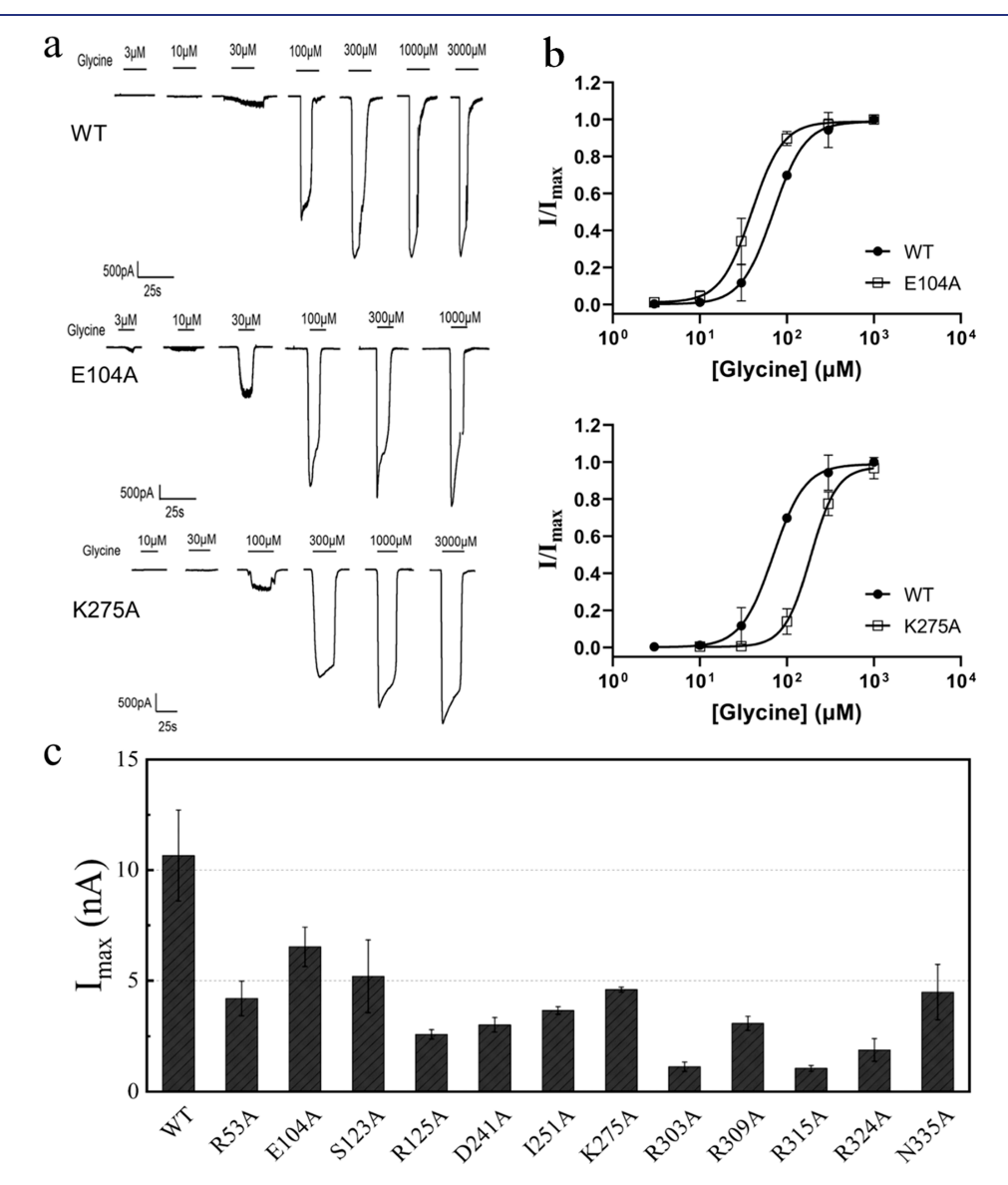


Figure 8. Functional characterization of predicted mutations by whole-cell patch clamp recording. (a) Sample whole-cell current recording for the wild type, E104A, and K275A mutants. Horizontal bars denote the duration of glycine application at concentrations illustrated in μ M. (b) The averaged whole-cell glycine dose response curve for the E104 and K275A mutants. Data is expressed as the mean \pm SEM from three experiments. (c) The maximal current amplitudes for the wild type and 12 mutants.

allowing Cl⁻ ions to pass through. These mutations disrupted the stable binding of glycine and inhibited chloride ion conduction. In addition, the positively charged residues R53, K275, R303, R309, R315, and R324 were within the Cl⁻ ion conduction path. Mutation to alanine can disrupt the positively charged electrostatic environment, inhibiting negatively charged chloride conduction (Figure 6b,c). Conversely, mutation of the negatively charged residue D278 on the permeation pathway decreases the electrostatic repulsion toward negative ions and facilitates Cl⁻ ion conduction

(Figure 6b). D241 formed multiple hydrogen bonds with A242 and R303, while the mutation disrupts these interactions (Figure 6d). Similarly, alanine mutations at I251 and N335 also disrupted multiple polar interactions between them and nearby amino acid residues (Figure 6e,f). The disruption of strong interaction caused by the mutation of important residues to alanine notably decreases the stability of GlyRs in the open state, thus impeding the conduction of Cl⁻ ions.

Experimental Validation of the Computationally Predicted Mutational Effects. To verify our hypothesis,

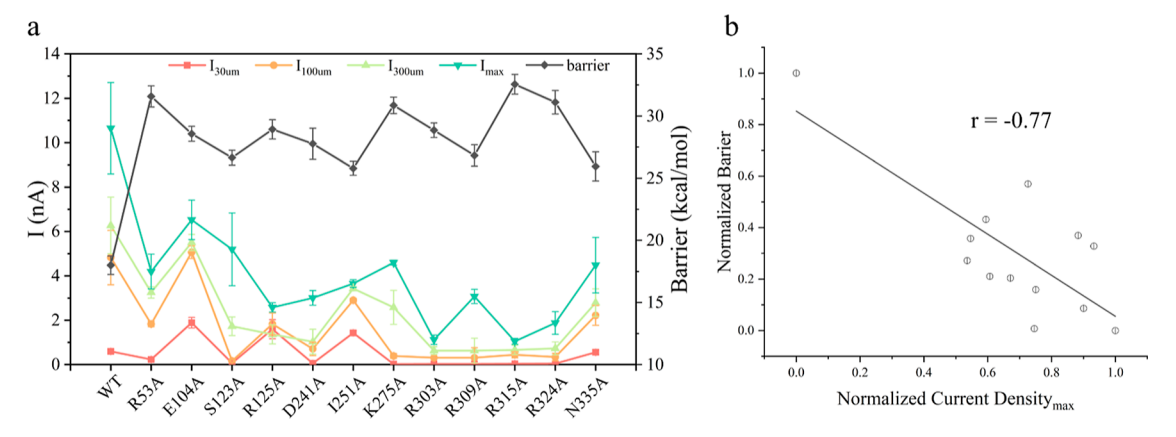


Figure 9. Comparison between computational and electrophysiological experimental results for cell lines that can generate glycine-induced currents. (a) Current magnitudes at different concentrations of glycine and maximum current amplitudes; computational free energy barriers. All data is shown as mean ± SEM. (b) Correlation analysis between the normalized energy barriers of the calculations and normalized maximum current amplitudes. The black line is derived from the linear fitting.

we conducted Western blotting and patch clamp experiments. For the wild type and 15 predicted mutant systems, we established the cell lines to check whether the predicted mutations of GlyRs are successfully expressed, and then analyzed the expression of these proteins by Western blotting. The results suggested that all mutant proteins were normally expressed in HEK293T cells (Figure 7). Subsequently, we employed patch clamp electrophysiology technique to determine the functional effects of the wild type and 15 mutations. All cell lines generated currents in whole cell patch clamp recordings, except for R113A, E151A, and D278A mutations. It was postulated these three mutations might cause the formation of nonfunctional channels analogous to the dominant T265I mutational protein, 16 whose signals are barely discernible. Consequently, these three mutations were excluded from the subsequent analyses.

To gain greater insight into the effects of the mutations on GlyR function, we used whole-cell patch clamp electrophysiology to record steady-state currents at a holding potential of -70 mV after GlyRs were activated by varying glycine concentrations for the wild type and 12 mutants. Figure 8a,b illustrate representative results of currents at homomeric α1 GlyRs, accompanied by the averaged glycine doseresponse relationship (complete results are provided in Figures S8 and S9). The figures suggest that the sensitivity to glycine was modestly enhanced in the case of the E104A mutants and diminished in the case of the K275A mutants, relative to the wild-type receptors.

All mutations changed glycine sensitivity with EC50 values presented in Table S3, while the specific mechanism that determines the glycine sensitivity of GlyRs is not clear in this field. The dominant mutations commonly disrupt the allosteric signal transduction pathway linking glycine binding to chloride channel gating, resulting in an apparent decrease in glycine sensitivity. 18,88 The 12 mutants that can be activated by glycine all showed higher free energy barriers and lower current magnitudes than those of the wild type. In most circumstances, the glycine sensitivity decreased compared to that of the wild type of GlyRs (Table S3). It was reasonable since they also affected signal transduction from glycine binding to GlyR channel gating, similar to the known mutations, which is consistent with our computational results. On the contrary, E104A, R125A, I251A mutants exhibited a dramatically

enhanced glycine sensitivity, and R309A and N335A mutants showed a slight increase in glycine sensitivity (Table S3). The mutation sites for E104A and R125A mutants were in the glycine binding sites (Figure S7); the mutations would increase the pocket size and make glycine easier to reach into the binding pocket, increasing glycine sensitivity. Although S123 was also in the glycine binding pocket (Figure S7), the mutation from serine to alanine for the mutant S123A made little change to the pocket size but still affected signal conduction. Thus, S123A mutant exhibited much weaker glycine sensitivity compared to E104A and R125A mutants (Table S3). Furthermore, the mutations to alanine of I251 in the lower part of the M2 helix (Figure S7) would enlarge the narrow tunnel pore size to allow conduction of Cl⁻ at low glycine concentrations, showing increased glycine sensitivity. R309A and N335A mutants might work like the R414H mutant¹⁸ in that they are all located in the M4 helix and have a relatively small effect on glycine sensitivity when impeding the function of GlyRs. Therefore, the subtle glycine sensitivity changes of R309A and N335A mutants would occur because they disrupted the function of GlyRs by a low rate of spontaneous activity more than affecting the signal transduction pathway of GlyRs, which is highly similar to that of the R414R mutant. 18 Despite the above-mentioned explanations about glycine sensitivity changes in mutants disrupting the GlyR function, further investigations are needed to explore the determinants in glycine sensitivity change.

We obtained the maximum current amplitudes for all cell lines (Figure 8c), which were used to represent the function of all cell lines and assess the accuracy of our predictions on mutation directions (inhibiting or facilitating). The maximum current amplitude in the wild-type cell line was the highest among all cell lines. This finding suggests that all mutants impeded chloride conduction in the channel pore, consistent with our predicted mutational directions, except for several mutants (R113A, E151A, and D178A) that generated no glycine-induced currents up to a saturated glycine concentration and might form nonfunctional channels. Consequently, for the mutants that can be activated by glycine, our predictions regarding the directions of the mutations (inhibiting or facilitating the function of GlyRs) were all correct.

To validate our predictions of the strength of the mutational effects, we depicted the current magnitudes at different concentrations of glycine and the maximum current amplitudes. We then compared the current magnitudes with energy barrier calculations. The results indicated that at the same concentration of glycine, the current magnitude of each mutation was much less than that in the wild type in most circumstances. Exceptions occurred when [glycine] = 30 μ M for E104A, R125A, I251A, and N335A mutants, or when [glycine] = 100 μ M for E104A mutants. The primary reason for this discrepancy was the difference in sensitivity between the mutants and the wild type of GlyR. The EC50 values for the E104A, R125A, I251A, and N335A mutants were smaller than the EC50 values for the wild type (Table S3), indicating that the mutants were more sensitive to glycine. At low glycine concentrations, E104A, R125A, I251A, and N335A mutants were more easily to be activated. However, the current magnitudes in higher glycine concentrations and the maximum current amplitudes for all mutants were weaker than those of the wild type of GlyRs. This further indicated that the chloride ion conductance of GlyRs was inhibited in these mutants. The calculated free energy barriers for Cl- ion conduction are shown in Figure 9a. In principle, a higher barrier indicates a stronger inhibition of GlyR function and a weaker current magnitude. Consequently, a higher computational barrier indicates a weaker current magnitude. In our calculations, the computed free energy barriers and recorded current magnitudes are highly correlated. For example, the maximum current magnitude was observed in the wild type, whereas the computed barrier was the lowest in all calculations. The R315A and R324A mutants exhibited lower current magnitudes and expected higher barriers.

To evaluate the computed mutational effect strength, we performed a correlation analysis by linearly fitting the normalized free energy barriers of our calculations to the normalized maximum current magnitudes in experiments according to eq 1.

$$X_{\text{normalized}} = \frac{(X - X_{\text{minimum}})}{(X_{\text{maximum}} - X_{\text{minimum}})}$$
(1)

Here, $X_{\rm maximum}$ and $X_{\rm minimum}$ represent the largest and smallest free energy barriers (or maximum current magnitudes) in the wild type of GlyR and all the mutants respectively; thus, the values for $X_{\rm maximum}$ and $X_{\rm minimum}$ are constant in all calculations. The results presented in Figure 9b demonstrate a negative correlation between the current magnitudes and energy barriers, with a Pearson's correlation coefficient of -0.77. This result indicates a robust correlation between our prediction and the electrophysiological results, validating the reliability of our predictions regarding mutational effect strength.

Considering that many mutational sites were along the ion permeation pathway, the free energy changes of binding of Clions to GlyR ($\Delta G_{\rm chloride\ ion}$) in the activation barrier might be highly related to the change of maximum current amplitudes. We calculated $\Delta G_{\rm chloride\ ion}$ in the intermediate to transition state conversion in the lateral pathway (I_2"-T_2" conversion) for the wild type of GlyR and all the mutants, and compared them with $I_{\rm max}$ (Figure S10). The $\Delta G_{\rm chloride\ ion}$ for all the mutants was larger than that in the wild type of GlyR, which was consistent with our experimental result (Figure S10a). However, the correlation result between the normalized $\Delta G_{\rm chloride\ ion}$ and

normalized $I_{\rm max}$ was not ideal, yielding a value of -0.55 (Figure S10b). These results are reasonable since the activation and Cl $^-$ ion conduction in GlyR are complex processes affected by multiple factors, while the activation energy barrier contained much information. Therefore, the correlation performance between the normalized activation energy barriers and the normalized maximum current amplitudes was better. Nevertheless, $\Delta G_{\rm chloride\ ion}$ still played a vital role in the prediction of mutational effects from the perspective of mutational direction and strength.

DISCUSSION

Previous studies have demonstrated that the open duration of GlyRs is prolonged for higher concentrations of glycine, which has led to the conclusion that any number of glycine molecules, from one to five, can activate GlyRs with varying efficiencies. S5,57,58,60 Nevertheless, these observations have not yet been quantitatively explained based on structural and energy considerations. In this study, we investigated the activation and desensitization behaviors of GlyRs with different glycine binding patterns, focusing on the change in the free energy barriers upon glycine binding. These results showed that an increase in glycine concentration facilitated the activation while impeding desensitization of GlyRs. When the number of bound glycine molecules is greater than or equal to three (binding at nonconsecutive sites), an efficacious opening of $\alpha 1$ GlyRs can be achieved.

Another major aspect of this study was the Cl ion conduction selectivity between the apical and lateral pathways. Although previous studies have proposed that the lateral pathway is the main conduction path, 63 a detailed explanation for this phenomenon from a structural and energetic perspective is lacking. A CG model capable of reliably describing the electrostatic energetics was used, enabling the creation of free energy surfaces of the coupled conformational change and ion conduction. Our investigation of the interrelationship between conformational and conductive processes indicates that the differential energy barrier heights between intermediate to transition state conversion in the apical pathway $(I_1''-T_1'')$ conversion, 22.0 kcal/mol) and the conversion in the lateral pathway $(I_2''-T_2'')$ conversion, 18.0 kcal/mol) result in ion conduction favoring the lateral pathway. Furthermore, the local electrostatic potential surface results and residue contribution analysis have shown that the electrostatic environment plays a pivotal role in this process.

By studying the underlying mechanisms, we could predict the mutational effects of the key residues located in the permeation pathway, glycine binding sites, and important loop regions (M2-M3 loop of the TMD). The mutational effects were assessed by focusing on the change in the highest free energy barrier in the intermediate to transition state conversion in the lateral pathway $(I_2''-T_2'')$ conversion upon the mutation of the target residue to alanine. The results suggested that mutations R53A, E104A, R113A, S123A, R125A, E151A, D241A, I251A, K275A, R303A, R309A, R315A, R324A, and N335A inhibited GlyR function, whereas mutation D278A facilitated chloride conduction. Among all the residues, E104A, R113A, S123A, R125A, and E151A were in the glycine binding pockets. R53A was in the β sheet of ECD, K275 was in the M2-M3 loop, and other residues were in the TMD. Our predictions for the known dominant hyperekplexia mutation sites were consistent with previous experimental results. Predictions were validated for several new single-point

mutation sites using patch clamp experiments. It is encouraging to note that the predictions regarding the directions of the mutational effects were all correct for the mutants that can be activated by glycine. Furthermore, the Pearson's correlation coefficient between the normalized free energy barriers of our calculations and the normalized maximum current magnitudes in experiments was -0.77, proving that our predictions of mutational effect strength were relatively reliable.

Despite the above-mentioned explorations, there were still certain limitations in our work. For the computational methods, we calculated the highest energy barrier changes of mutants to predict mutational effects from direction and strength perspectives. The method worked well for loss-offunction mutants, while for the gain-of-function mutant we predicted (D278A), which was later proved to be a nonfunctional mutant in the experimental work, our prediction was unsuccessful. Thus, it needs further improvement. In addition, in free energy calculation, the systems in the wild type of GlyR and all the mutants were relaxed by MD runs at 300 K before free energy calculation, until the energy reached convergence (energy basically stopped falling). The relaxation time was approximately 1 ns in the conformational free energy calculation and 6 ns in glycine and chloride ion binding free energy calculations. Nevertheless, the relaxation time might not be enough for the mutant K275A, as the mutational site was located in the GlyR loop regions and probably had an allosteric effect on ion conduction. The movement of loops might be large if the simulation is much longer, while shorttime simulations cannot consider the large movement of loops and would constrain the energy in the local minimum. Moreover, our computational calculation only considered single ion conduction in the ion permeation pathway. However, the scenario is much more complex. Ion permeation in GlyR might be a multi-ion process, which can be deduced by the fact that two chloride ions coexist in the TMD in one of the pLGICs.³⁷ Therefore, ion-ion interactions should be considered in this circumstance. Future work should take into account ion-ion interactions in the Cl- ion conduction of GlyRs.

METHODS

Modeling of the End Point State Structures and Calculation of the Thermodynamic Cycle. End point state structures of zebrafish $\alpha 1$ glycine receptor were obtained from the PDB as follows: 6plz (closed state), 6ply (open state), and 6plx (desensitized state). We used the Targeted MD method (Supporting Information) to generate a series of intermediate structures for each of the two end point state structures. Subsequently, conformational changes were observed in the closed-open-desensitized-closed state cycle. The model was solvated using a surface-constrained all-atom solvent (SCAAS)⁸⁹ sphere with a radius of 38 Å. The water molecules are represented by Langevin dipoles. The surface-constrained water sphere region was surrounded by a 2 Å Langevin dipole. Long-range electrostatic effects were analyzed using the local reaction field (LRF) method.⁹⁰ Each system consisted of approximately 35,000 atoms. Energy minimization was applied to each system, including 10,000 steps for the steepest descent algorithm and 10,000 steps for the conjugate gradient algorithm. Each system was then relaxed with the NVT ensemble at 310 K using a Langevin thermostat until the energy reached convergence (energy basically stops falling). The relaxation time was approximately 1 ns and the time step was 2 fs. These structures were then trimmed to CG models of ~24,000 atoms. The protonation states of each residue were determined using the Monte Carlo-Proton Transfer (MCPT) algorithm, ⁶⁹ and a lattice of unified

atoms representing membrane particles were added to the system. The inclusion of ions may be significant in all-atom free energy calculations, but is not relevant to our CG free energy calculations because the CG model includes an effective dielectric that accounts for the energetics. The next relaxation run was performed (time step: 2 fs; simulation time: 3 ns) before evaluating the CG free energy profiles of the conformational changes. Molaris-XG software ^{91,92} was used with the ENZYMIX force field ^{69,91} for all calculations.

Binding Free Energy Calculation between GlyRs and Glycine Molecules. For each intermediate structure, we docked glycine molecules in the pockets based on the corresponding binding associations using Audock Vina⁹³ and selected the conformation with the highest score. A relaxation run (time step of 2 fs, simulation time of 6 ns, and temperature of 310 K) was performed to ensure the energy reached convergence (energy basically stops falling) before calculating the binding free energy between glycine and GlyRs. Subsequently, we used the PDLD/S-LRA method, ^{78,80} as described in Supporting Information, for binding free energy calculations. Molaris-XG software ^{91,92} was used for the relaxation runs and PDLD/S-LRA calculations.

Binding Free Energy Calculation between GlyRs and Chloride Ions in 2D Free Energy Landscape. To investigate chloride ion conduction, we employed Molaris-XG software 91,95 dock chloride ions at various positions within the channel pore, with a spacing of 2 Å in each intermediate structure. In total, 57 and 43 chloride ion conduction structures were constructed for the apical and lateral pathways, respectively, from the extracellular entrance to the intracellular exit in each intermediate state. The binding free energy between the chloride ions and GlyR was calculated using the Poisson-Boltzmann linear response approximation (PB-LRA) method. Before the binding energy calculation between chloride ions and GlyRs, a relaxation run (time step of 2 fs, simulation time of 6 ns, and temperature of 310 K) for each system was performed to ensure the energy reached convergence (energy basically stops falling). After the coupling of the CG conformational energy and binding free energy of the five glycine molecules, we generated free energy maps of chloride conduction in the apical and lateral pathways. All calculations were performed using Molaris-XG software.

Mutational Effects. We assessed the mutational effects based on barrier changes between the wild-type and GlyR mutants. We calculated the barrier for the wild type using eq 2, the barrier for the mutant with eq 3, and the barrier changes by eq 4.

Farrier_{WT} =
$$(\Delta G_{\text{fold}} + \Delta G_{\text{glycine}}^{\text{PDLD/S-LRA/}\beta} + \Delta G_{\text{Cl}}^{\text{PDLD/S-LRA/}\beta})_{\text{T}_{2}^{"}\text{WT}} - (\Delta G_{\text{fold}} + \Delta G_{\text{glycine}}^{\text{PDLD/S-LRA/}\beta} + \Delta G_{\text{Cl}}^{\text{PDLD/S-LRA/}\beta})_{\text{I}_{2}^{"}\text{WT}}$$
(2)

$$\begin{aligned} \text{Barrier}_{\text{MT}} &= \\ & \left(\Delta G_{\text{fold}} + \Delta G_{\text{glycine}}^{\text{PDLD/S-LRA/}\beta} + \Delta G_{\text{Cl}}^{\text{PDLD/S-LRA/}\beta} \right)_{\text{T}_{2}^{'},\text{MT}} \\ & - \left(\Delta G_{\text{fold}} + \Delta G_{\text{glycine}}^{\text{PDLD/S-LRA/}\beta} + \Delta G_{\text{Cl}}^{\text{PDLD/S-LRA/}\beta} \right)_{\text{I}_{2}^{'},\text{MT}} \end{aligned} \tag{3}$$

$$\Delta Barrier = Barrier_{MT} - Barrier_{WT}$$
 (4)

where T_2'' and I_2'' are the transition and intermediate states respectively, as shown in Figure 4d. The energy at each point includes the protein folding energy, glycine binding energy, and Cl^- ion binding energy.

Cell Culture and Cell Line Established. HEK293T cells (Cell Bank of Shanghai Institute of Life Sciences, Chinese Academy of Sciences) were maintained in Dulbecco's modified Eagle's medium (DMEM) (Invitrogen) supplemented with 100 U/mL penicillin and 10% fetal bovine serum (FBS). The cells were then grown in an incubator at 37 °C with 15% relative humidity and 5% CO₂. To obtain HEK293T cells stably expressing human GlyR α 1 subunits (wild type and all mutant types), the cell lines were transfected with a PiggyBac Transposase plasmid. After approximately 72 h, the cells

were transferred to a medium containing puromycin (1 mg/mL) to select positive clones, which were then subjected to a ten-day selection process.

Electrophysiology Patch Clamping. We conducted whole-cell patch clamp recordings of GlyR currents in human embryonic kidney 293 (HEK293) cells. All the patch clamp experiments were performed at 25 °C. Borosilicate glass capillaries (BF150-80-10, 1.5 mm \times 0.86 mm) were used to prepare the electrodes. The electrodes exhibited a resistance of 2–4 MΩ when filled with the internal pipette solution. Currents were recorded using a HEKA EPC10 (Germany). The current was sampled at 20 kHz.

The internal pipette solution comprised the following components (in mM): 135 KCl, 2 MgCl2, 1 EGTA, 10 HEPES, 4 Mg-ATP, 0.3 Na-GTP, and KOH (adjusted to a pH of 7.4). The external solution comprised the following (in mM): 140 mM NaCl, 4 mM KCl, 1.8 mM CaCl₂, 1 mM MgCl₂, 10 mM glucose, 10 mM HEPES, and NaOH (pH 7.4).

The effects of varying concentrations of glycine (ranging from 1 to 3000 μ M) were investigated by recording glycine-gated currents at a holding potential of -70 mV. The data was processed using Igor software. The half-maximal concentration (EC50) values were calculated for each glycine concentration—response relationship using the Hill equation, which was fitted by a nonlinear least-squares analysis (GraphPad Prism 5.0). Three experiments were conducted for each mutant and wild-type sample.

ASSOCIATED CONTENT

Supporting Information

The Supporting Information is available free of charge at https://pubs.acs.org/doi/10.1021/jacs.4c08489.

Additional details and results; CG model, MCPT algorithm, and the calculation process of folding free energy; plasmid construction and transfection process; western blotting; CG model of the α 1 GlyR from different views; residue energy contributions in the process of conformational changes; residue energy contributions of glycine binding effects; residue energy contributions of Cl- ion binding effects; alanine scanning calculations for the residues that may influence GlyR function; locations of E104, S123, E125, I251, N335, and R309 in GlyRs; whole-cell patch-clamp recordings for the wild type of GlyRs and all the mutants; averaged whole-cell glycine dose-response curves; decomposition of free energy of conformational changes for I₁-T₂ and open-T4 barriers; free energy profiles in I_1'' , T_1'' states of the "gly5" curve; free energy in three states (closed, open, and desensitized states) and energy changes (ΔG) in different glycine binding patterns; EC50 values of the wild type/mutations of GlyRs; and primer sequences (PDF)

AUTHOR INFORMATION

Corresponding Authors

Luonan Chen – Key Laboratory of Systems Biology, Institute of Biochemistry and Cell Biology, Center for Excellence in Molecular Cell Science, Chinese Academy of Sciences, Shanghai 200031, China; Email: lnchen@sibcb.ac.cn

Arieh Warshel — Department of Chemistry, University of Southern California, Los Angeles, California 90089-1062, United States; orcid.org/0000-0001-7971-5401; Email: warshel@usc.edu

Chen Bai — School of Medicine, Warshel Institute for Computational Biology, The Chinese University of Hong Kong, Shenzhen 518172, China; College of Pharmaceutical Sciences, Zhejiang University, Hangzhou 310058, China; Chenzhu (MoMeD) Biotechnology Co., Ltd., Hangzhou 310005, China; orcid.org/0000-0003-4560-3019; Email: baichen@momedtech.com.cn

Author

Junfang Yan – School of Medicine, Warshel Institute for Computational Biology, The Chinese University of Hong Kong, Shenzhen 518172, China

Complete contact information is available at: https://pubs.acs.org/10.1021/jacs.4c08489

Notes

The authors declare no competing financial interest.

ACKNOWLEDGMENTS

This research was supported by the National Natural Science Foundation of Youth Fund Project (grant number: 22103066); 2021 Basic Research General Project of ShenZhen, China (grant number: 20210316202830001); the Pearl River Talent Fund of Guangdong Province (grant number: 2021QN020539); and the Warshel Institute for Computational Biology funding from Shenzhen City and Longgang District (LGKCSDPT2024001). A.W. is supported by the National Institutes of Health R35 GM122472 and the National Science Foundation Grant MCB 1707167.

REFERENCES

- (1) Dent, J. A. The Evolution of Pentameric Ligand-Gated Ion Channels; Adv Exp Med Biol, 2010; Vol. 683, pp 11-23.
- (2) daCosta, C. J.; Baenziger, J. E. Gating of pentameric ligand-gated ion channels: structural insights and ambiguities. *Structure* **2013**, *21* (8), 1271–1283.
- (3) Nemecz, A.; Prevost, M. S.; Menny, A.; Corringer, P. J. Emerging Molecular Mechanisms of Signal Transduction in Pentameric Ligand-Gated Ion Channels. *Neuron* **2016**, *90* (3), 452–470.
- (4) Lycksell, M.; Rovšnik, U.; Hanke, A.; Martel, A.; Howard, R. J.; Lindahl, E. Biophysical characterization of calcium-binding and modulatory-domain dynamics in a pentameric ligand-gated ion channel. *Proc. Natl. Acad. Sci. U.S.A.* **2022**, *119* (50), No. e2210669119.
- (5) Lynch, J. W. Molecular structure and function of the glycine receptor chloride channel. *Physiol. Rev.* **2004**, *84* (4), 1051–1095.
- (6) Dutertre, S.; Becker, C. M.; Betz, H. Inhibitory glycine receptors: an update. *J. Biol. Chem.* **2012**, 287 (48), 40216–40223.
- (7) Kasaragod, V. B.; Schindelin, H. Structure—Function Relationships of Glycine and GABAA Receptors and Their Interplay With the Scaffolding Protein Gephyrin. *Front. Mol. Neurosci.* **2018**, *11*, 317.
- (8) Zhang, Z. Y.; Bai, H. H.; Guo, Z.; Li, H. L.; He, Y. T.; Duan, X. L.; Suo, Z. W.; Yang, X.; He, Y. X.; Hu, X. D. mGluR5/ERK signaling regulated the phosphorylation and function of glycine receptor α 1ins subunit in spinal dorsal horn of mice. *PLoS Biol.* **2019**, *17* (8), No. e3000371.
- (9) Colquhoun, D. Binding, gating, affinity and efficacy: the interpretation of structure-activity relationships for agonists and of the effects of mutating receptors. *Br. J. Pharmacol.* **1998**, *125* (5), 923–947.
- (10) Howard, R. J. Elephants in the Dark: Insights and Incongruities in Pentameric Ligand-gated Ion Channel Models. *J. Mol. Biol.* **2021**, 433 (17), 167128.
- (11) Liu, J.; Wu, D. C.; Wang, Y. T. Allosteric potentiation of glycine receptor chloride currents by glutamate. *Nat. Neurosci.* **2010**, *13* (10), 1225–1232.
- (12) Beech, R. N.; Neveu, C. The evolution of pentameric ligand-gated ion-channels and the changing family of anthelmintic drug targets. *Parasitology* **2015**, *142* (2), 303–317.

- (13) Breitinger, U.; Breitinger, H. G. Modulators of the Inhibitory Glycine Receptor. ACS Chem. Neurosci. 2020, 11 (12), 1706–1725.
- (14) Gallagher, C. I.; Ha, D. A.; Harvey, R. J.; Vandenberg, R. J. Positive Allosteric Modulators of Glycine Receptors and Their Potential Use in Pain Therapies. *Pharmacol. Rev.* **2022**, 74 (4), 933–961.
- (15) Ivica, J.; Zhu, H.; Lape, R.; Gouaux, E.; Sivilotti, L. G. Aminomethanesulfonic acid illuminates the boundary between full and partial agonists of the pentameric glycine receptor. *Elife* **2022**, *11*, No. e79148.
- (16) Chung, S. K.; Vanbellinghen, J. F.; Mullins, J. G.; Robinson, A.; Hantke, J.; Hammond, C. L.; Gilbert, D. F.; Freilinger, M.; Ryan, M.; Kruer, M. C.; Masri, A.; Gurses, C.; Ferrie, C.; Harvey, K.; Shiang, R.; Christodoulou, J.; Andermann, F.; Andermann, E.; Thomas, R. H.; Harvey, R. J.; Lynch, J. W.; Rees, M. I. Pathophysiological mechanisms of dominant and recessive GLRA1 mutations in hyperekplexia. *J. Neurosci.* 2010, 30 (28), 9612–9620.
- (17) Bode, A.; Wood, S. E.; Mullins, J. G. L.; Keramidas, A.; Cushion, T. D.; Thomas, R. H.; Pickrell, W. O.; Drew, C. J. G.; Masri, A.; Jones, E. A.; Vassallo, G.; Born, A. P.; Alehan, F.; Aharoni, S.; Bannasch, G.; Bartsch, M.; Kara, B.; Krause, A.; Karam, E. G.; Matta, S.; Jain, V.; Mandel, H.; Freilinger, M.; Graham, G. E.; Hobson, E.; Chatfield, S.; Vincent-Delorme, C.; Rahme, J. E.; Afawi, Z.; Berkovic, S. F.; Howell, O. W.; Vanbellinghen, J. F.; Rees, M. I.; Chung, S. K.; Lynch, J. W. New hyperekplexia mutations provide insight into glycine receptor assembly, trafficking, and activation mechanisms. *J. Biol. Chem.* **2013**, 288 (47), 33745–33759.
- (18) Bode, A.; Lynch, J. W. The impact of human hyperekplexia mutations on glycine receptor structure and function. *Mol. Brain* 2014. 7. 2.
- (19) Wilkins, M. E.; Caley, A.; Gielen, M. C.; Harvey, R. J.; Smart, T. G. Murine startle mutant Nmf11 affects the structural stability of the glycine receptor and increases deactivation. *J. Physiol.* **2016**, *594* (13), 3589–3607.
- (20) Schaefer, N.; Berger, A.; van Brederode, J.; Zheng, F.; Zhang, Y.; Leacock, S.; Littau, L.; Jablonka, S.; Malhotra, S.; Topf, M.; Winter, F.; Davydova, D.; Lynch, J. W.; Paige, C. J.; Alzheimer, C.; Harvey, R. J.; Villmann, C. Disruption of a Structurally Important Extracellular Element in the Glycine Receptor Leads to Decreased Synaptic Integration and Signaling Resulting in Severe Startle Disease. *J. Neurosci.* 2017, 37 (33), 7948–7961.
- (21) Vergouwe, M. N.; Tijssen, M. A.; Peters, A. C.; Wielaard, R.; Frants, R. R. Hyperekplexia phenotype due to compound heterozygosity for GLRA1 gene mutations. *Ann. Neurol.* **1999**, *46* (4), 634–638.
- (22) Safar, F.; Hurdiss, E.; Erotocritou, M.; Greiner, T.; Lape, R.; Irvine, M. W.; Fang, G.; Jane, D.; Yu, R.; Damgen, M. A.; Biggin, P. C.; Sivilotti, L. G. The Startle Disease Mutation E103K Impairs Activation of Human Homomeric α1 Glycine Receptors by Disrupting an Intersubunit Salt Bridge across the Agonist Binding Site. J. Biol. Chem. 2017, 292 (12), 5031–5042.
- (23) Aboheimed, G. I.; AlRasheed, M. M.; Almudimeegh, S.; Peña-Guerra, K. A.; Cardona-Londoño, K. J.; Salih, M. A.; Seidahmed, M. Z.; Al-Mohanna, F.; Colak, D.; Harvey, R. J.; Harvey, K.; Arold, S. T.; Kaya, N.; Ruiz, A. J. Clinical, genetic, and functional characterization of the glycine receptor β -subunit A455P variant in a family affected by hyperekplexia syndrome. *J. Biol. Chem.* **2022**, 298 (7), 102018.
- (24) Beato, M.; Groot-Kormelink, P. J.; Colquhoun, D.; Sivilotti, L. G. The Activation Mechanism of α1 Homomeric Glycine Receptors. *J. Neurosci.* **2004**, 24 (4), 895–906.
- (25) Bregman, H.; Simard, J. R.; Andrews, K. L.; Ayube, S.; Chen, H.; Gunaydin, H.; Guzman-Perez, A.; Hu, J.; Huang, L.; Huang, X.; Krolikowski, P. H.; Lehto, S. G.; Lewis, R. T.; Michelsen, K.; Pegman, P.; Plant, M. H.; Shaffer, P. L.; Teffera, Y.; Yi, S.; Zhang, M.; Gingras, J.; DiMauro, E. F. The Discovery and Hit-to-Lead Optimization of Tricyclic Sulfonamides as Potent and Efficacious Potentiators of Glycine Receptors. *J. Med. Chem.* 2017, 60 (3), 1105–1125.
- (26) Huang, N.; Wang, Y.; Zhan, G.; Yu, F.; Li, S.; Hua, D.; Jiang, R.; Li, S.; Wu, Y.; Yang, L.; Zhu, B.; Hua, F.; Luo, A.; Yang, C.

- Contribution of skeletal muscular glycine to rapid antidepressant effects of ketamine in an inflammation-induced mouse model of depression. *Psychopharmacology (Berl.)* **2019**, 236 (12), 3513–3523.
- (27) Zhang, Z. Y.; Guo, Z.; Li, H. L.; He, Y. T.; Duan, X. L.; Suo, Z. W.; Yang, X.; Hu, X. D. Ubiquitination and inhibition of glycine receptor by HUWE1 in spinal cord dorsal horn. *Neuropharmacology* **2019**, *148*, 358–365.
- (28) Meyer, G.; Kirsch, J.; Betz, H.; Langosch, D. Identification of a gephyrin binding motif on the glycine receptor β subunit. *Neuron* **1995**, *15* (3), 563–572.
- (29) Zhu, H.; Gouaux, E. Architecture and assembly mechanism of native glycine receptors. *Nature* **2021**, *599* (7885), 513-517.
- (30) Du, J.; Lu, W.; Wu, S.; Cheng, Y.; Gouaux, E. Glycine receptor mechanism elucidated by electron cryo-microscopy. *Nature* **2015**, *526* (7572), 224–229.
- (31) Bormann, J.; Hamill, O. P.; Sakmann, B. Mechanism of anion permeation through channels gated by glycine and gamma-amino-butyric acid in mouse cultured spinal neurones. *J. Physiol.* **1987**, *385*, 243–286.
- (32) Gielen, M.; Corringer, P. J. The dual-gate model for pentameric ligand-gated ion channels activation and desensitization. *J. Physiol.* **2018**, 596 (10), 1873–1902.
- (33) Keramidas, A.; Moorhouse, A. J.; French, C. R.; Schofield, P. R.; Barry, P. H. M2 pore mutations convert the glycine receptor channel from being anion- to cation-selective. *Biophys. J.* **2000**, *79* (1), 247–259.
- (34) Keramidas, A.; Moorhouse, A. J.; Pierce, K. D.; Schofield, P. R.; Barry, P. H. Cation-selective mutations in the M2 domain of the inhibitory glycine receptor channel reveal determinants of ion-charge selectivity. *J. Gen. Physiol.* **2002**, *119* (5), 393–410.
- (35) Harpole, T. J.; Grosman, C. Side-chain conformation at the selectivity filter shapes the permeation free-energy landscape of an ion channel. *Proc. Natl. Acad. Sci. U.S.A.* **2014**, *111* (31), E3196–E3205.
- (36) Cymes, G. D.; Grosman, C. Identifying the elusive link between amino acid sequence and charge selectivity in pentameric ligand-gated ion channels. *Proc. Natl. Acad. Sci. U.S.A.* **2016**, *113* (45), E7106–E7115.
- (37) Hibbs, R. E.; Gouaux, E. Principles of activation and permeation in an anion-selective Cys-loop receptor. *Nature* **2011**, 474 (7349), 54–60.
- (38) Rossokhin, A. V.; Zhorov, B. S. Side chain flexibility and the pore dimensions in the GABAA receptor. *J. Comput. Aided Mol. Des.* **2016**, 30 (7), 559–567.
- (39) Keramidas, A.; Lynch, J. W. An outline of desensitization in pentameric ligand-gated ion channel receptors. *Cell. Mol. Life Sci.* **2013**, 70 (7), 1241–1253.
- (40) Gielen, M.; Thomas, P.; Smart, T. G. The desensitization gate of inhibitory Cys-loop receptors. *Nat. Commun.* **2015**, *6*, 6829.
- (41) Huang, X.; Chen, H.; Michelsen, K.; Schneider, S.; Shaffer, P. L. Crystal structure of human glycine receptor- α 3 bound to antagonist strychnine. *Nature* **2015**, 526 (7572), 277–280.
- (42) Huang, X.; Shaffer, P. L.; Ayube, S.; Bregman, H.; Chen, H.; Lehto, S. G.; Luther, J. A.; Matson, D. J.; McDonough, S. I.; Michelsen, K.; Plant, M. H.; Schneider, S.; Simard, J. R.; Teffera, Y.; Yi, S.; Zhang, M.; DiMauro, E. F.; Gingras, J. Crystal structures of human glycine receptor α3 bound to a novel class of analgesic potentiators. *Nat. Struct. Mol. Biol.* **2017**, 24 (2), 108–113.
- (43) Kumar, A.; Basak, S.; Rao, S.; Gicheru, Y.; Mayer, M. L.; Sansom, M. S. P.; Chakrapani, S. Mechanisms of activation and desensitization of full-length glycine receptor in lipid nanodiscs. *Nat. Commun.* **2020**, *11* (1), 3752.
- (44) Yu, J.; Zhu, H.; Lape, R.; Greiner, T.; Du, J.; Lü, W.; Sivilotti, L.; Gouaux, E. Mechanism of gating and partial agonist action in the glycine receptor. *Cell* **2021**, *184* (4), 957–968.e21.
- (45) Kumar, A.; Kindig, K.; Rao, S.; Zaki, A. M.; Basak, S.; Sansom, M. S. P.; Biggin, P. C.; Chakrapani, S. Structural basis for cannabinoid-induced potentiation of alpha1-glycine receptors in lipid nanodiscs. *Nat. Commun.* **2022**, *13* (1), 4862.

- (46) Gibbs, E.; Klemm, E.; Seiferth, D.; Kumar, A.; Ilca, S. L.; Biggin, P. C.; Chakrapani, S. Conformational transitions and allosteric modulation in a heteromeric glycine receptor. *Nat. Commun.* **2023**, *14* (1), 1363.
- (47) Shi, S.; Lefebvre, S. N.; Peverini, L.; Cerdan, A. H.; Milán Rodríguez, P.; Gielen, M.; Changeux, J. P.; Cecchini, M.; Corringer, P. J. Illumination of a progressive allosteric mechanism mediating the glycine receptor activation. *Nat. Commun.* **2023**, *14* (1), 795.
- (48) Huang, X.; Chen, H.; Shaffer, P. L. Crystal Structures of Human GlyR α 3 Bound to Ivermectin. *Structure* **2017**, 25 (6), 945–950.e2.
- (49) Yu, H.; Bai, X. C.; Wang, W. Characterization of the subunit composition and structure of adult human glycine receptors. *Neuron* **2021**, *109* (17), 2707–2716.e6.
- (50) Prevost, M. S.; Moraga-Cid, G.; Van Renterghem, C.; Edelstein, S. J.; Changeux, J. P.; Corringer, P. J. Intermediate closed state for glycine receptor function revealed by cysteine cross-linking. *Proc. Natl. Acad. Sci. U.S.A.* **2013**, *110* (42), 17113–17118.
- (51) Burzomato, V.; Beato, M.; Groot-Kormelink, P. J.; Colquhoun, D.; Sivilotti, L. G. Single-Channel Behavior of Heteromeric $\alpha 1\beta$ Glycine Receptors: An Attempt to Detect a Conformational Change before the Channel Opens. *J. Neurosci.* **2004**, 24 (48), 10924–10940.
- (52) Lape, R.; Colquhoun, D.; Sivilotti, L. G. On the nature of partial agonism in the nicotinic receptor superfamily. *Nature* **2008**, 454 (7205), 722–727.
- (53) Krashia, P.; Lape, R.; Lodesani, F.; Colquhoun, D.; Sivilotti, L. G. The long activations of $\alpha 2$ glycine channels can be described by a mechanism with reaction intermediates ("flip"). *J. Gen. Physiol.* **2011**, 137 (2), 197–216.
- (54) Scott, S.; Lynch, J. W.; Keramidas, A. Correlating structural and energetic changes in glycine receptor activation. *J. Biol. Chem.* **2015**, 290 (9), 5621–5634.
- (55) Fucile, S.; de Saint Jan, D.; David-Watine, B.; Korn, H.; Bregestovski, P. Comparison of glycine and GABA actions on the zebrafish homomeric glycine receptor. *J. Physiol.* **1999**, *517* (2), 369–383.
- (56) Miller, P. S.; Topf, M.; Smart, T. G. Mapping a molecular link between allosteric inhibition and activation of the glycine receptor. *Nat. Struct. Mol. Biol.* **2008**, *15* (10), 1084–1093.
- (57) Beato, M.; Groot-Kormelink, P. J.; Colquhoun, D.; Sivilotti, L. G. Openings of the Rat Recombinant α 1 Homomeric Glycine Receptor as a Function of the Number of Agonist Molecules Bound. *J. Gen. Physiol.* **2002**, *119* (5), 443–466.
- (58) Jackson, M. B.; Wong, B. S.; Morris, C. E.; Lecar, H.; Christian, C. N. Successive openings of the same acetylcholine receptor channel are correlated in open time. *Biophys. J.* **1983**, *42* (1), 109–114.
- (59) Colquhoun, D.; Sakmann, B. Fast events in single-channel currents activated by acetylcholine and its analogues at the frog muscle end-plate. *J. Physiol.* **1985**, 369, 501–557.
- (60) Twyman, R. E.; Macdonald, R. L. Kinetic properties of the glycine receptor main- and sub-conductance states of mouse spinal cord neurones in culture. *J. Physiol.* **1991**, *435*, 303–331.
- (61) Colquhoun, D.; Hatton, C. J.; Hawkes, A. G. The quality of maximum likelihood estimates of ion channel rate constants. *J. Physiol.* **2003**, *547* (3), *699*–728.
- (62) Sivilotti, L. G. What single-channel analysis tells us of the activation mechanism of ligand-gated channels: the case of the glycine receptor. *J. Physiol.* **2010**, *588* (1), 45–58.
- (63) Cerdan, A. H.; Peverini, L.; Changeux, J. P.; Corringer, P. J.; Cecchini, M. Lateral fenestrations in the extracellular domain of the glycine receptor contribute to the main chloride permeation pathway. *Sci. Adv.* **2022**, 8 (41), No. eadc9340.
- (64) Cerdan, A. H.; Martin, N.; Cecchini, M. An Ion-Permeable State of the Glycine Receptor Captured by Molecular Dynamics. *Structure* **2018**, *26* (11), 1555–1562.e4.
- (65) Dämgen, M. A.; Biggin, P. C. A Refined Open State of the Glycine Receptor Obtained via Molecular Dynamics Simulations. *Structure* **2020**, 28 (1), 130–139.e2.

- (66) Fan, Z. Z.; Hwang, J. K.; Warshel, A. Using simplified protein representation as a reference potential for all-atom calculations of folding free energy. *Theor. Chem. Acc.* **1999**, *103* (1), 77–80.
- (67) Messer, B. M.; Roca, M.; Chu, Z. T.; Vicatos, S.; Kilshtain, A. V.; Warshel, A. Multiscale simulations of protein landscapes: using coarse-grained models as reference potentials to full explicit models. *Proteins* **2010**, 78 (5), 1212–1227.
- (68) Vicatos, S.; Rychkova, A.; Mukherjee, S.; Warshel, A. An effective coarse-grained model for biological simulations: recent refinements and validations. *Proteins* **2014**, *82* (7), 1168–1185.
- (69) Vorobyov, I.; Kim, I.; Chu, Z. T.; Warshel, A. Refining the treatment of membrane proteins by coarse-grained models. *Proteins* **2016**, 84 (1), 92–117.
- (70) Lee, M.; Kolev, V.; Warshel, A. Validating a Coarse-Grained Voltage Activation Model by Comparing Its Performance to the Results of Monte Carlo Simulations. *J. Phys. Chem. B* **2017**, *121* (50), 11284–11291.
- (71) Warshel, A.; Sharma, P. K.; Kato, M.; Parson, W. W. Modeling electrostatic effects in proteins. *Biochim. Biophys. Acta* **2006**, *1764* (11), 1647–1676.
- (72) Bai, C.; Wang, J.; Mondal, D.; Du, Y.; Ye, R. D.; Warshel, A. Exploring the Activation Process of the β 2AR-G_sComplex. *J. Am. Chem. Soc.* **2021**, *143* (29), 11044–11051.
- (73) Bai, C.; Warshel, A. Revisiting the protomotive vectorial motion of F(0)-ATPase. *Proc. Natl. Acad. Sci. U.S.A.* **2019**, *116* (39), 19484–19489.
- (74) Bai, C.; Asadi, M.; Warshel, A. The catalytic dwell in ATPases is not crucial for movement against applied torque. *Nat. Chem.* **2020**, *12* (12), 1187–1192.
- (75) Bai, C.; Warshel, A. Critical Differences between the Binding Features of the Spike Proteins of SARS-CoV-2 and SARS-CoV. J. Phys. Chem. B 2020, 124 (28), 5907–5912.
- (76) Bai, C.; Wang, J.; Chen, G.; Zhang, H.; An, K.; Xu, P.; Du, Y.; Ye, R. D.; Saha, A.; Zhang, A.; Warshel, A. Predicting Mutational Effects on Receptor Binding of the Spike Protein of SARS-CoV-2 Variants. J. Am. Chem. Soc. 2021, 143 (42), 17646–17654.
- (77) Schlitter, J.; Engels, M.; Krüger, P. Targeted molecular dynamics: a new approach for searching pathways of conformational transitions. *J. Mol. Graph.* **1994**, *12* (2), 84–89.
- (78) Muegge, I.; Tao, H.; Warshel, A. A fast estimate of electrostatic group contributions to the free energy of protein-inhibitor binding. *Protein Eng.* **1997**, *10* (12), 1363–1372.
- (79) Schutz, C. N.; Warshel, A. What are the dielectric "constants" of proteins and how to validate electrostatic models? *Proteins* **2001**, *44* (4), 400–417.
- (80) Singh, N.; Warshel, A. Absolute binding free energy calculations: on the accuracy of computational scoring of protein-ligand interactions. *Proteins* **2010**, *78* (7), 1705–1723.
- (81) Rao, S.; Klesse, G.; Stansfeld, P. J.; Tucker, S. J.; Sansom, M. S. P. A BEST example of channel structure annotation by molecular simulation. *Channels* **2017**, *11* (4), 347–353.
- (82) Alhadeff, R.; Warshel, A. Simulating the function of sodium/proton antiporters. *Proc. Natl. Acad. Sci. U.S.A.* **2015**, *112* (40), 12378–12383.
- (83) Zhang, Y.; Wu, K.; Li, Y.; Wu, S.; Warshel, A.; Bai, C. Predicting Mutational Effects on Ca(2+)-Activated Chloride Conduction of TMEM16A Based on a Simulation Study. *J. Am. Chem. Soc.* **2024**, *146* (7), 4665–4679.
- (84) Smart, O. S.; Neduvelil, J. G.; Wang, X.; Wallace, B. A.; Sansom, M. S. HOLE: a program for the analysis of the pore dimensions of ion channel structural models. *J. Mol. Graph.* **1996**, *14* (6), 354–360.
- (85) Paulino, C.; Kalienkova, V.; Lam, A. K. M.; Neldner, Y.; Dutzler, R. Activation mechanism of the calcium-activated chloride channel TMEM16A revealed by cryo-EM. *Nature* **2017**, *552* (7685), 421–425.
- (86) Tian, Y.; Chen, S.; Shan, Q. Charged residues at the pore extracellular half of the glycine receptor facilitate channel gating: a

- potential role played by electrostatic repulsion. J. Physiol. 2020, 598 (20), 4643-4661.
- (87) Harvey, R. J.; Topf, M.; Harvey, K.; Rees, M. I. The genetics of hyperekplexia: more than startle. *Trends Genet.* **2008**, 24 (9), 439–447.
- (88) Rajendra, S.; Lynch, J. W.; Pierce, K. D.; French, C. R.; Barry, P. H.; Schofield, P. R. Startle disease mutations reduce the agonist sensitivity of the human inhibitory glycine receptor. *J. Biol. Chem.* **1994**, 269 (29), 18739–18742.
- (89) King, G.; Warshel, A. A surface constrained all-atom solvent model for effective simulations of polar solutions. *J. Chem. Phys.* **1989**, *91*, 3647–3661.
- (90) Lee, F. S.; Warshel, A. A local reaction field method for fast evaluation of long-range electrostatic interactions in molecular simulations. *J. Chem. Phys.* **1992**, *97*, 3100–3107.
- (91) Lee, F. S.; Chu, Z. T.; Warshel, A. Microscopic and semimicroscopic calculations of electrostatic energies in proteins by the POLARIS and ENZYMIX programs. *J. Comput. Chem.* **1993**, *14* (2), 161–185.
- (92) Kamerlin, S. C.; Vicatos, S.; Dryga, A.; Warshel, A. Coarsegrained (multiscale) simulations in studies of biophysical and chemical systems. *Annu. Rev. Phys. Chem.* **2011**, *62*, 41–64.
- (93) Trott, O.; Olson, A. J. AutoDock Vina: improving the speed and accuracy of docking with a new scoring function, efficient optimization, and multithreading. *J. Comput. Chem.* **2010**, 31 (2), 455–461.